



# One year of aerosol refractive index measurement from a coastal Antarctic site

Zsófia Jurányi<sup>1,a</sup> and Rolf Weller<sup>1</sup>

<sup>1</sup>Alfred-Wegener-Institut Helmholtz Zentrum für Polar- und Meeresforschung, Bremerhaven, Germany

<sup>a</sup>now at: Institute for the Protection of Maritime Infrastructures, German Aerospace Center (DLR), Bremerhaven, Germany

**Correspondence:** Zsófia Jurányi (zsofia.juranyi@gmail.com)

**Abstract.** Climate change model evaluations need a better understanding of the atmospheric aerosols' optical properties and with this of the refractive index (RI) of atmospheric aerosols as well. Due to the remoteness of Antarctica only a very few data on the refractive index exists from there. In this paper we calculate the real refractive index of atmospheric aerosols from number size distribution measurements at a coastal Antarctic measurement site. In our calculations we used the overlapping  
5 size range (120–340 nm) of a scanning mobility sizer (SMPS), which sizes the particles by their electrical mobility, and a laser aerosol spectrometer (LAS), which sizes the particles by their optical scattering signal.

Based on almost a complete year of measurement and 2439 measurement points, the average effective refractive index ( $RI_{\text{eff}}$ ) turned out to be 1.44. This is in a good agreement with the RI value of 1.47 which we derived from the chemical composition filter measurements. At our measurement site the aerosol has a very characteristic seasonal pattern in both number  
10 concentration and chemical composition. Despite this, we could not identify any significant seasonal variability in the  $RI_{\text{eff}}$ , the monthly averages remain within the range of 1.40–1.50. Two austral winter months June and September has a slightly higher average values (1.50 and 1.47).

We could not identify any influence of the occurring wind direction on the retrieved  $RI_{\text{eff}}$  either. For the few examples of north winds coming from the Neumayer station (occurs very rarely, this is the reason why the measurement site was built to  
15 the south), we don't see different values than for the other wind directions. During an artificial, high contamination episode, when diesel engines were operated right next to the measurement site, we had an hour of constant conditions such that one RI fit was possible. This fit resulted in an unusual high RI of 1.59, which is most probably due to the high black carbon content of the diesel engine emission. Therefore, we also assume that even during northerly wind directions we did not have significant influence from the Neumayer station.

20 During a shorter period between 2017 December and 2018 January we used the time averaged LAS and SMPS number size distributions to get some information on the size dependency of the refractive index. The  $RI_{\text{eff}}$  was fit in 5 different particle size ranges, and we have found a slight decrease of the  $RI_{\text{eff}}$  with the particle size from 1.47 in the 116–168 nm to 1.37 in the 346–478 nm range.



## 1 Introduction

Atmospheric aerosols affect the radiative balance of planet Earth (e.g. Ramanathan et al., 2001): directly by absorbing and scattering the sunlight (Schwartz, 1996) and indirectly through modifying the micro-physical properties of the clouds (Lohmann and Feichter, 2005). The current state of the scientific knowledge on the total (direct and indirect) aerosol effect is still considered low due to the complexity of these effects (IPCC, 2014).

The refractive index (RI) of the atmospheric aerosols is a key parameter calculating their absorption and scattering and therefore essential for the global modeling of the aerosol's radiative effects. There are more existing optical software packages for the optical properties of the atmospheric particulate matter and these packages extensively use RI values of the different kind of aerosols. The OPAC (Optical Properties of Aerosols and Clouds, Hess et al., 1998) package is based on laboratory measurements, whereas the HITRAN-RI (High-resolution TRANsmiission Refractive Indices, Massie and Hervig, 2013) package uses both laboratory and field measurements for the different included components and allows comparisons between the products using the different RIs as well. Valenzuela et al. (2018) showed us that there is still clearly a need for additional and accurate measurements of the RI.

The most common method to determine the RI of aerosol particles is an indirect method: the measurement of the absorption and/or scattering of the particles along with the knowledge of the particle's size. The absorption and the scattering of a single particle is determined by the particle's size, shape and RI. It is most often assumed that particles are spherical and for the theoretical calculations the Mie theory can be used.

Wex et al. (2009) determined the RI of secondary organic aerosol by selecting the particle size using a differential mobility analyser (DMA) and measuring the scattering signal using an optical particle counter (OPC). The same method was used by Hand and Kreidenweis (2002) on ambient aerosol, additionally they combined the measurements from an aerodynamic particle sizer as well, in order to gain information on the particles' density. Bukowiecki et al. (2011); Zhang et al. (2013); Zieger et al. (2015) used the number size distribution with parallel nephelometer and aethalometer measurements to determine the RI of ambient aerosols. A very similar method was used by Virkkula et al. (2006), where it was assumed that the imaginary part of the RI can be neglected and therefore no absorption data was used.

Barkey et al. (2007) measured laboratory generated particles' number size distribution and parallel their light scattering by a polar nephelometer. They introduced an inversion algorithm to obtain the RI. A new and more exotic method is to use optical trapping combined with Mie spectroscopy to capture the RI of atmospheric aerosol samples in the 460–700 nm wavelength range by Shepherd et al. (2018). Cavity ring-down spectroscopy is a commonly used method to study the light extinction by aerosol particles. This was used by Bluvshstein et al. (2012) who introduced an RI retrieval method by measuring the light extinction at two carefully selected size parameters.

As we see there are plenty of existing measurements on aerosol RI, but the majority of these measurements are on laboratory generated particles and only less on ambient aerosols. And if we look for RI measurements from Antarctica we can only find very few available data. Hogan et al. (1979) collected aerosol particles at the South Pole in a size range between 0.3 and 12  $\mu\text{m}$  during a 4-days period and put oils with known different RIs on them until the particles disappeared. They have found an RI



of 1.54 for these samples. Virkkula et al. (2006) derived the RI of the ambient aerosol at coastal Antarctica during a 12-days summer campaign and got values around 1.43–1.44. Insoluble organic aerosol collected at the Clean Air Sector Laboratory of the British Antarctic station Halley was analysed by Shepherd et al. (2018). The samples were collected on 60 consecutive days during the austral summer of 2015 and they got an RI of 1.47.

- 5 In this paper we would like to present continuous data on the real RI at 633 nm wavelength of the ambient aerosol as derived from measurements of an optical particle counter and a scanning mobility particle sizer. To our knowledge this is the first time, that such long-term RI measurements of almost one year from Antarctica is presented.

## 2 Method

### 2.1 Sampling Site

- 10 The measurements presented in this paper were performed in the Air Chemistry Observatory (SPUSO from "Spurenstoffob-  
servatorium") of the German Antarctic station of Neumayer III. The SPUSO is situated at the coast of Antarctica on the  
Ekström shelfice close to the Atka Bay. This observatory is a global site of the WHO's Global Atmosphere Watch programme  
(World Meteorological Organisation, 2016). Detailed description of the site and of the prevailing meteorological conditions  
were already presented elsewhere (Wagenbach et al., 1988; Weller et al., 2008), here we only give a brief introduction to the  
15 site.

- The SPUSO lies 1.5 km south from the Neumayer station and stays on the shelf-ice which moves approximately 120 m  
every year to the north. The edge of the shelf-ice and with this the sea is 7-to-21 km to the north. Due to the remoteness of  
the measurement site, anthropogenic pollution can barely reach it, the main aerosol source is the Southern Ocean. During the  
austral summer the sea next to the shelf ice edge and in the close Atka bay is ice free, whereas during the long antarctic winter  
20 the next open water can be as far as 100 km. Towards the inside of the continent, apart from some nunataks there is no ice-free  
surface.

- The only possible contamination source is the Neumayer station itself, where most of the energy is provided by diesel  
engines. This is the reason why the SPUSO was built 1.5 km to the south of the station in a clean air sector and its power  
supply is provided through a cable from the main station. At this measurement site, northerly winds are almost never present  
25 and therefore most of the time we can have a contamination free sampling. The Neumayer station is completely isolated and  
not reachable during the winter season which lasts 9 months.

### 2.2 Experimental Setup

- At our measurement site, the aerosol is continuously sampled through our inlet system, which has its air intake approximately  
8 m above the snow surface. The inlet has an aerodynamic cut-off diameter of 7–10  $\mu\text{m}$  at windspeeds of 4–10  $\text{ms}^{-1}$  (Weller  
30 et al., 2008). Due to the heated measurement container and the low ambient temperatures, aerosol entering the measurement  
container is dry ( $\text{RH} < 30\%$ , most of the time even  $\text{RH} < 10\%$ ) without any additional drying. The inlet system is made of



electropolished stainless steel, the individual instruments are connected to the inlet via stainless steel as well or/and conductive silicon tubing.

The particle number size distribution was measured with two commercial instruments. A scanning mobility particle sizer (SMPS) consisting of an electrostatic classifier (TSI 3080) and a condensational particle counter (CPC, TSI 3776) measured in the 16–960 nm particle mobility diameter range. The SMPS was operated with  $2.2 \text{ L min}^{-1}$  sheath flow and  $0.3 \text{ L min}^{-1}$  sample flow. Next to the SMPS a laser aerosol spectrometer (LAS, TSI 3340) was installed as well. This instrument detects and sizes the particles by measuring the intensity of their scattered light as they pass by the 633 nm Helium-Neon active cavity laser. The optical design and the high laser intensity makes the detection of single particles down to 90 nm diameter possible. The sample flow of the LAS was set to  $0.05 \text{ L min}^{-1}$ , the sheath flow was  $0.65 \text{ L min}^{-1}$ . The instrument measured in the size range of 90–5000 nm and was factory calibrated by Polystyrene Latex (PSL) particles. Both the SMPS and LAS measured with a 10-minutes time resolution, however the LAS and the SMPS sees different particles at a time. The LAS counts all the particles which pass by its laser beam whereas the SMPS performed two scans within the 10-minutes time period and only able to detect one particle size at the time, dependent on the voltage that is currently set in the instrument. Therefore if the aerosol changes significantly within 10 minutes, differences can exist between the measurements of the two instruments as well.

The particle number concentration was measured by a commercial CPC (CPC, TSI 3775) with a one-minute time resolution. A Multi-Angle Absorption Photometer (MAAP, Thermo ESM Andersen) operating at a wavelength of 630 nm (Petzold and Schönlinner, 2004) was used to measure the BC mass concentration during the measurement campaign. The absorption values were converted into BC mass concentration using a mass absorption efficiency of  $6.6 \text{ m}^2 \text{ g}^{-1}$ , and were registered also once in a minute. The ionic composition of the aerosol is measured by a low volume Teflon/Nylon filter system, and the filters are analysed by ion chromatography. The filters were changed daily but not every day at the same time and therefore the time resolution of the ionic composition varies with the time. The average sampling flow was  $\approx 3.5 \text{ m}^3 \text{ h}^{-1}$ , the sampled air volume varied between  $30 \text{ m}^3$  and  $125 \text{ m}^3$  in 2017. The filter sampling is automatically switched off in case of a possible contamination (snow drift, wind coming from the Neumayer station, low windspeed, too high particle concentration or too high windspeed), see details in Weller et al. (2008). In this study we used the following main ionic species:  $\text{NH}_4^+$ ,  $\text{Na}^+$ ,  $\text{NO}_3^-$ , non sea-salt  $\text{SO}_4^{2-}$  and  $\text{MSA}^-$  (methanesulphonate). The CPC, the MAAP and the filter measurements are part of the continuous measurement program of GAW.

### 2.3 Correction of the LAS losses

We have collected data from both the LAS and SMPS instruments for almost one year (09.02.2017–20.01.2018). Unfortunately, during most of this time, the LAS was positioned horizontally too far away (ca. 3 m) from the inlet such, that significant amount of particles were lost in the connecting tube. This problem was first discovered in November 2017. Right after, on the 23.11.2017, the instrument was repositioned right below the inlet in order to minimize the particle losses. We used the number size distribution data in the diameter range between 120 and 340 nm (see section 2.6) for the RI determination, therefore it was important to check whether or not we are able to correct for the particle losses before November 2017 in this diameter range.

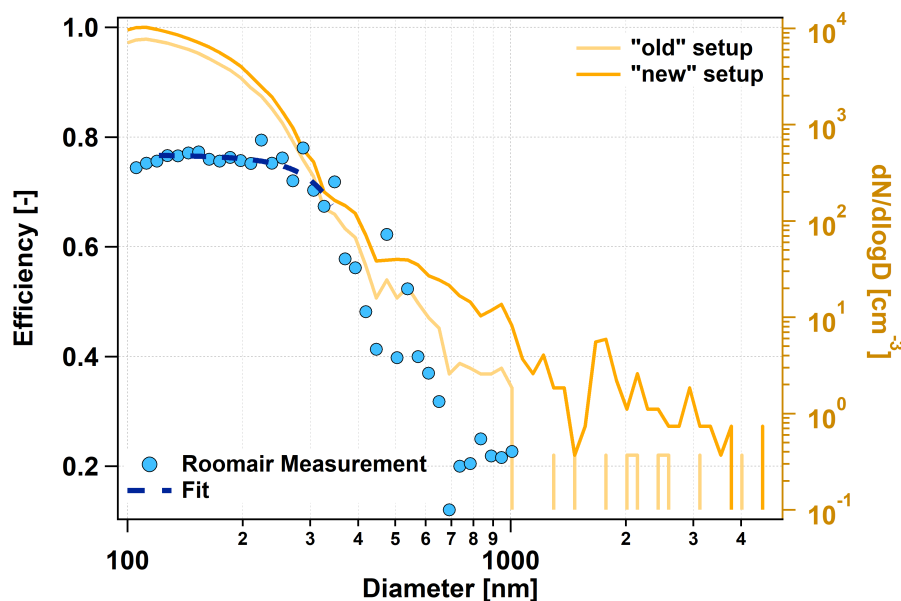


**Figure 1.** The quantification of the LAS losses in the sampling line. The two orange lines belong to the right axis and show the average room air number size distributions. "Old" setup: time average with the long horizontal tube, "new" setup: time average without the horizontal tube. The blue dots show the penetration efficiency through the tube, the dashed dark blue line shows a polynomial fit in the diameter range which was used for the RI calculation.

Measuring the losses in the sampling line which was used before November 2017 ("old" setup) was a challenging task. Our measurement site, the SPUSO, did not have any kind of particle generator to perform tests with, and due to the location and isolation of the station, it was also impossible to receive any equipment for the test. Our best option was to use the room air of the measurement container to quantify the losses. This particle source provided only a low concentration such, that more hours of measurement were needed. One measurement cycle included the number size distribution measurement with the LAS of the room air aerosol in the "old" setup and right after removing the horizontal tube another measurement in the "new" setup, with the shorter, vertical tube. To make sure, that the aerosol source is stable enough during one cycle, the setup was changed every 60 s.

All measured number size distributions were averaged separately for the "old" and the "new" setups, and the average number size distributions were compared. Figure 1 shows the results of this average number size distribution comparison. If one looks at it (Fig. 1, orange lines, right axis) or the penetration efficiency (Fig. 1, blue dots, left axis) it is obvious that the losses in the "old" sampling line are significant, almost all particles with diameters above 1  $\mu\text{m}$  were lost, and therefore it is impossible to make any correction there. This is the reason, why we only have the complete number size distribution until 5  $\mu\text{m}$  after November 2017 for this study. However, in the diameter range of the RI determination of 120–340 nm, the efficiency is between 0.77 and 0.67. The losses are significant here as well, but we consider this still as correctable. To have a continuous



correction factor, the efficiency (Fig. 1, blue dots) was fit with a polynomial line. The blue dashed line shows this polynomial fit which was used for the correction.

## 2.4 Time averaging

Due to the low aerosol number concentration in Antarctica we performed a base time averaging of one hour of all measured  
5 data. This one hour averaging still often resulted in too noisy number size distributions, such that an RI fit was impossible. The particle number concentration at our measurement site has a strong seasonal variability with much lower concentrations in winter than in summer. This is why we decided to perform on top of the one hour time averaging a particle concentration dependent time averaging as well in order to keep the time resolution as high as possible.

After performing many tests, we concluded, that the one hour averaged SMPS number size distributions, that were recorded  
10 during a time period with an average number concentration of at least  $400 \text{ cm}^{-3}$  had a good enough signal to noise ratio for the RI calculation and no further averaging was needed. For all other cases with lower concentrations the hourly averaged data was further averaged until the number of the detected particles by the SMPS equaled or exceeded the particle number detected during a one hour SMPS scan with  $400 \text{ cm}^{-3}$  concentration. With this averaging method in some extreme cases in winter the measured data had to be averaged for 15 hours, whereas in summer most of the time the original one hour or maybe  
15 2-hours averaging time was needed. Due to this averaging method we have the highest possible time resolution but it is not constant, changing in time. This changing time resolution had to be taken into account for all further time average or statistical calculations.

## 2.5 Recalculation of the LAS number size distribution

The LAS is factory calibrated using PSL particles having an RI of 1.588 (Eidhammer et al., 2008). In order to be able to  
20 recalculate the particle number size distribution to any other RI, we need to calculate the theoretical instrument response (TIR, the signal which the instrument measures) of the LAS for both PSL and the desired particle RI as function of the particle diameter. This was done by a custom-written Mie code using the LAS wavelength of  $\lambda = 633 \text{ nm}$  and a detection angle  $\Theta$  between 22 and 158 degrees with a geometry of a round detector shape.

The LAS diameter bin boundaries corresponding to the PSL calibration can be transformed to a diameter at the target RI by  
25 searching for the PSL calibration TIR value in the TIR values calculated with the target RI and looking up the corresponding diameter. However, this problem is not always straight-forward, because OPCs using a monochromatic laser often suffer from a non-monotonic instrument response at higher diameters (e.g., Hodkinson and Greenfield, 1965; Barnard and Harrison, 1988).

This problem of non-monotonic instrument response was solved by smoothing the calculated instrumental response function. The smoothing was done by fitting a 5<sup>th</sup> grade polynomial to the logarithm of both PSL and target RI TIR functions. Figure 2  
30 shows an example how a single bin boundary diameter ( $D_{30}$ , the 30<sup>th</sup> diameter bin border) is recalculated using another ( $m = 1.4 + 0i$ ) RI. The Mie calculation (solid line) and the polynomial fit (dashed line) are shown for both RIs. The 30<sup>th</sup> diameter bin border is 592 nm in our setup, using the original PSL calibration. One can read from Figure 2 that a PSL particle of this size detected by the LAS results in the same TIR as a particle with the RI of 1.4 and the size of  $D'_{30} = 723 \text{ nm}$ . The same

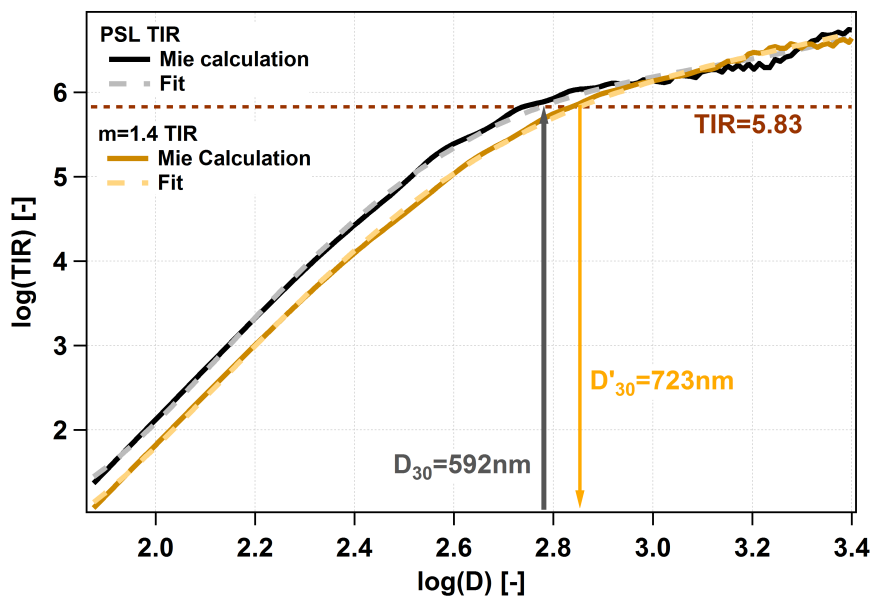


**Figure 2.** LAS Theoretical instrument responses for  $m = 1.588 + 0i$  (black) and  $1.40 + 0i$  (orange) as function of the particle diameter. Here we show an example, how an original LAS diameter bin border ( $D_{30}$ ) was recalculated to the target RI ( $D'_{30}$ ) is shown.

procedure has to be used for every bin boundary diameter and every desired index of refraction. After having the recalculated diameter borders, we can recalculate the number size distribution as well. If the original number size distribution is:

$$n(D) = \frac{dN(D)}{d\log(D)} \quad (1)$$

Then the recalculated number size distribution looks like this:

$$5 \quad n'(D') = \frac{dN(D')}{d\log(D')} = \frac{dN(D')}{\log(D'_{\text{high}}) - \log(D'_{\text{low}})} \quad (2)$$

where  $D'_{\text{high}}$  is the upper and  $D'_{\text{low}}$  is the lower boundary of the recalculated diameter bin.

## 2.6 Calculation of the effective refractive index

In order to find the aerosol refractive index, the SMPS and the LAS data has to be matched. This matching was done by recalculating the LAS number size distribution using a set of different RIs and finding the one which matches the best the



SMPS number size distribution at the overlapping size range. The following expression was used after Khlystov et al. (2004) to quantise the difference between the LAS and the SMPS distribution:

$$\chi(m) = \frac{1}{N} \cdot \sum_{i=N_{\min}}^{N_{\max}} [\log(n_{\text{SMPS}}(D_i)) - \log(n_{\text{LAS}}(m, D_i))]^2 \quad (3)$$

The SMPS and the LAS has an overlapping size range between 90 and 950 nm, however only the range between 120 and 340 nm was used for the fit due to the very low particle concentration. The SMPS number size distribution was too noisy over 340 nm and at the lowest diameters, the LAS does not have a detection efficiency of unity. The range of the RI was chosen to be 1.3–1.8 with 0.01 steps in between. The imaginary part of the RI was kept at 0 which is an acceptable assumption considering that the absorption is very low compared to the scattering at our measurement site, average single scattering albedo at Neumayer is 0.992 (Weller et al., 2013). The  $\chi(m)$  function was determined for every single  $m$  value and the aerosol RI is the  $m$  value where the  $\chi$  function reaches its minimum. Those cases were omitted where the  $\chi$  function did not have an explicit minimum or exceeded a limit. After manual inspection of many fit procedures this limit was set to the value of 0.02. Such cases might occur if too much noise is present in the data or if the size distribution was varying too much during the time period of one scan. Next to this numerical criterion every single scan was manually checked as well.

The RI derived with our method is representative for the used overlapping size range of 120–340 nm. If the chemical composition of the aerosol is changing with the particle size, it is also possible that the RI is also size dependent. This we have to keep in mind for later conclusions. The other assumption we use is that the aerosol particles are spherical and that the imaginary part of the RI is negligible. Due to these assumptions we call the derived RI the effective refractive index ( $\text{RI}_{\text{eff}}$ ).

### 3 Results and discussion

#### 3.1 Verification of the LAS correction

In order to verify the used LAS correction (see Sec. 2.3), measurements of particles with known RI and spherical shape was necessary. The lack of any particle generator left us with not many possibilities. A commercial e-cigarette (Joytech eGo) was available at the station, and we used this to generate particles for the testing purpose. E-cigarette liquid contains glycerin, propylene glycol, water, nicotine and flavourings and the formed aerosol particles are spherical liquid droplets. Pratte et al. (2016) measured the RI of many e-cigarettes of different types and got values between 1.429 and 1.436, and therefore we assume that our generated test particles had an RI of 1.43.

We filled a plastic bag of  $\approx 100$  L volume with particle free air then added 2–3 puffs of the e-cigarette smoke using a small, hand-operated air pump. After that, we let the aerosol particles coagulate in the bag for 10–15 min, in order to let the particles reach the size range of the RI calculation. The e-cigarette test was done with the same setup as the "old" measurement setup using the long vertical tube. We used the method introduced in the sections 2.5 and 2.6 to determine the RI of this e-cigarette smoke. For this fit we have chosen a slightly different particle size range of 110–220 nm because the form of the number size

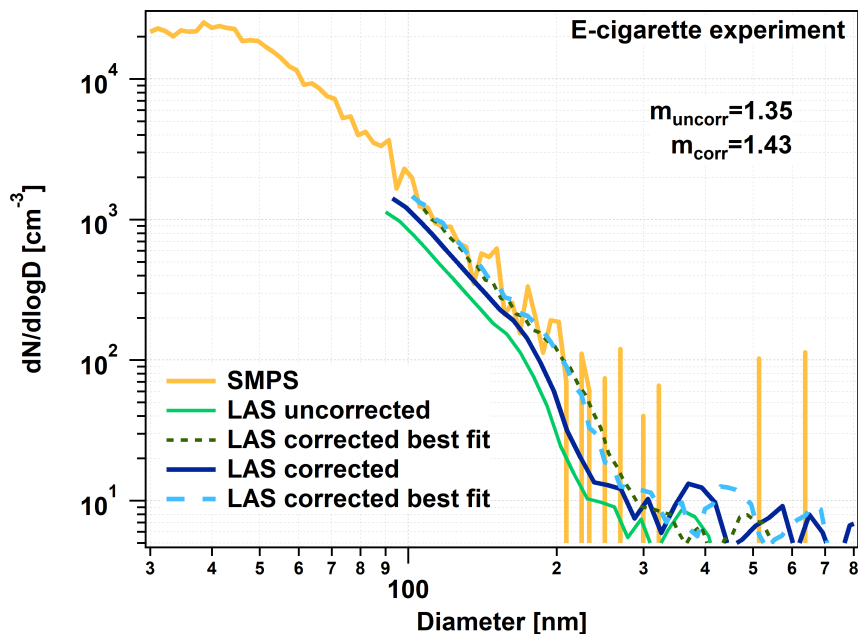


**Figure 3.** The E-cigarette experiment, showing the validation of our LAS correction. The orange line shows the measured SMPS number size distribution, the green lines the uncorrected LAS number size distribution (light: original, dark and dashed: best fit with  $m_{\text{uncorr}}$  calculated RI) and the blue lines (dark: original, light and dashed: best fit with  $m_{\text{corr}}$  calculated RI) are the losses corrected LAS number size distributions.

distribution was different from the ambient one. Figure 3 shows the results of the e-cigarette experiment. Without using the above mentioned correction on the LAS data (green lines) we get an RI of 1.35 from the best fit. This value is significantly lower than the literature RI value of 1.43 suggesting that the LAS losses have a high influence on the retrieved RI and that the correction is necessary. After applying the correction, the best fit between the SMPS and the LAS data (blue lines) was achieved at the RI of 1.43 which is in agreement with the literature value. This verifies our LAS correction, which was applied on all LAS data before November 2017.

### 3.2 Sensitivity of the RI calculation on the number size distribution measurement

The accuracy of our  $RI_{\text{eff}}$  calculation mainly depends on the measured input data's uncertainty, which is the uncertainty of the number size distribution measurements in our case. Here, we discuss the sensitivity of the derived  $RI_{\text{eff}}$  values introduced by the measurement uncertainty. An intercomparison between many mobility particle size spectrometers showed that all of the different investigated instruments measured within an uncertainty range of  $\pm 10\%$  (Wiedensohler et al., 2012). We use this value for our SMPS, and assume that the LAS has the same uncertainty as well.

In order to investigate the effect of this measurement uncertainty we take the worst case scenarios, by either adding 10% to the particle number concentration measured by the SMPS and subtract 10% from the LAS, or the other way around. We



calculated for one month of measurement period the  $RI_{\text{eff}}$  values using these modified number size distributions next to the original ones. Choosing 10% higher SMPS concentration and 10% lower LAS concentration resulted in lower calculated  $RI_{\text{eff}}$ . On average the values were 0.045 lower compared to the original values which translates into an average 3.1% error. The other scenario results in artificially high values, which turned out to be on average 0.050 and this means an error of 3.5%. This shows that even assuming the worst case scenario would cause an acceptable error, and most probably we can count with a lower uncertainty in reality.

### 3.3 RI calculation examples

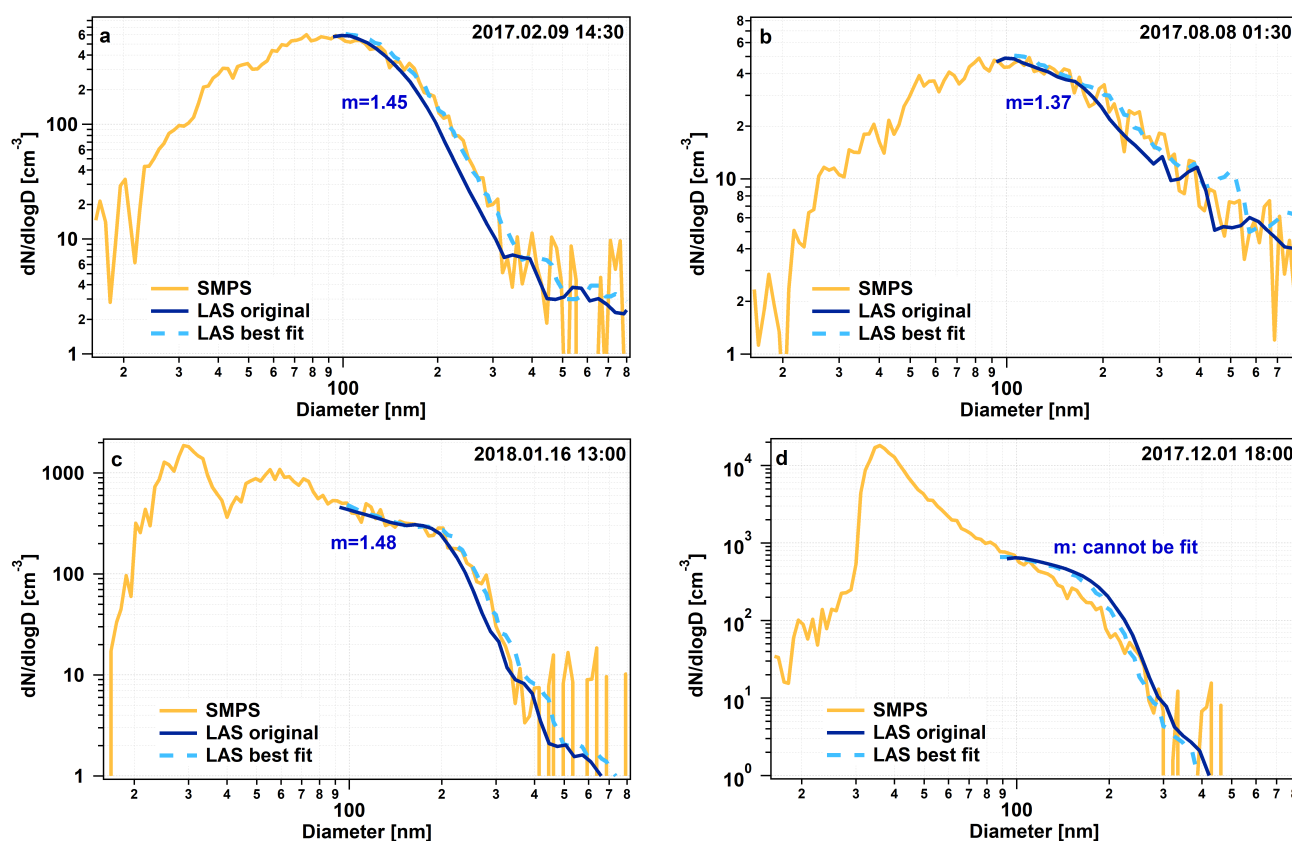


**Figure 4.** 4 examples on the refractive index fit performance. The orange line shows the measured SMPS number size distribution, whereas the blue lines (dark: original, light and dashed: best fit) show the LAS number size distributions.

Figure 4 shows four examples about the performance of the RI fitting procedure in different cases. The first snapshot of Figure 4a is from the summer season when the number concentration was high enough that no further averaging was necessary than the one-hour averaging. The orange line shows the measured SMPS scan whereas the dark blue line shows the simultaneously measured LAS number size distribution with the factory calibration. The dark blue line lies below the SMPS line which



indicates that the built-in calibration RI of 1.588 overestimates the prevailing RI. The fitting procedure verifies this and the best fit belongs to the recalculated LAS scan with the RI of 1.45 which we consider as the effective refractive index,  $RI_{\text{eff}}$  at that time point.

Figure 4b shows a similar situation from winter with much lower particle concentrations and therefore a longer averaging time of 11 hours. The obtained RI was quite low: 1.37 in this case. An uncommon example can be seen in figure 4c when the number size distribution was trimodal. The fit was successful this case as well, the retrieved RI is 1.48. As the last example (Fig. 4d), we show a case where the fit was unsuccessful, we could not retrieve a valid RI. The fitting procedure returned a best fit, but the value of  $\chi$  exceeded 0.02 and it is also clearly visible that this best solution does not fit very well the measured SMPS number size distribution. The reason why the fit did not work in this case was that the aerosol population was significantly changing within the duration of the SMPS scan. During the first half of the scan an aerosol plume with very high concentration reached the instruments. This was an extreme and exceptional situation where some construction was done around the SPUSO using machines powered by diesel engines.

### 3.4 Seasonal variability and mean value of the refractive index

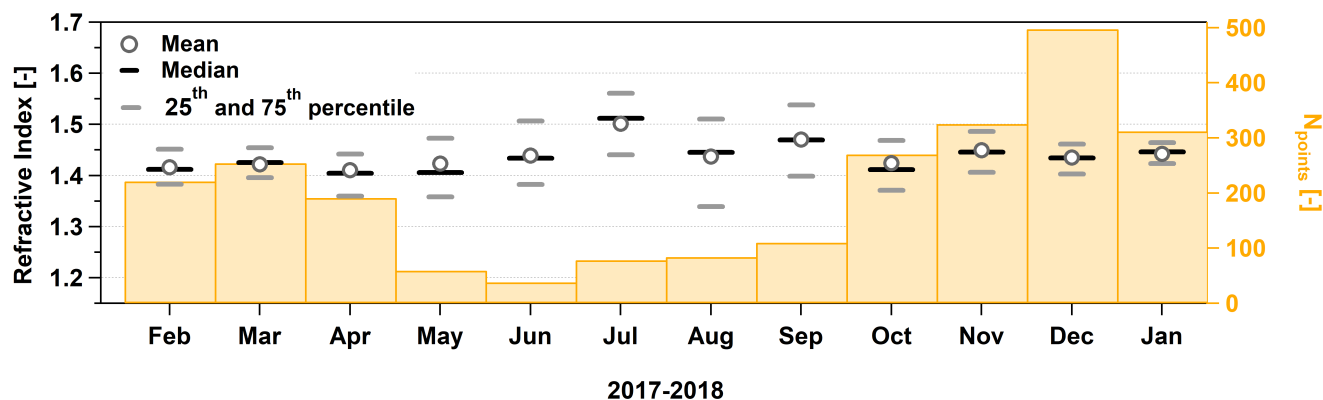


**Figure 5.** The monthly averages, medians and percentiles of the effective RI from the coastal Antarctica. The orange bars refer to the right axis and show the number of successful RI retrievals.

We have collected data during almost a complete year (from 09.02.2017 to 20.01.2018), and this gave us the unique possibility to calculate the long-term  $RI_{\text{eff}}$  and be able to analyze its seasonal variability. Figure 5 shows this seasonal variability, where the statistics of the monthly  $RI_{\text{eff}}$  is presented. The gray circles show the monthly mean values, the black sticks the medians and the gray sticks the 25<sup>th</sup> and 75<sup>th</sup> percentiles. The orange bar chart belongs to the right axis and indicates the number of the  $RI_{\text{eff}}$  values that could be retrieved for the according month. The same data is also shown in Table 1, and it is complemented with the yearly mean values as well.

The average  $RI_{\text{eff}}$  during our complete measurement period was 1.438 and the median is also close with the value of 1.414. As already mentioned, there are only a very few other RI measurements from Antarctica. Virkkula et al. (2006) calculated



**Table 1.** The monthly and yearly ( $\Sigma$ ) averages, medians and percentiles of the  $RI_{\text{eff}}$  from coastal Antarctica.

Month	25 <sup>th</sup> percentile	Median	75 <sup>th</sup> percentile	Mean	$N_{\text{points}}$
Feb	1.382	1.412	1.451	1.412	221
Mar	1.395	1.425	1.454	1.422	254
Apr	1.359	1.404	1.442	1.410	191
May	1.358	1.401	1.473	1.423	59
Jun	1.382	1.434	1.507	1.439	38
Jul	1.440	1.512	1.561	1.501	78
Aug	1.339	1.445	1.510	1.437	84
Sep	1.398	1.469	1.538	1.470	110
Oct	1.371	1.411	1.468	1.424	270
Nov	1.406	1.446	1.486	1.449	325
Dec	1.403	1.434	1.461	1.435	497
Jan	1.423	1.446	1.464	1.442	312
$\Sigma$	1.369	1.414	1.462	1.438	2439

the RI values from number size distribution and scattering coefficient measurements at the Finnish Antarctic summer station of Aboa. Aboa is situated approximately 300 km to the west of the Neumayer station and lies a little further away from the sea. These measurements were performed in the summer of 2000 during a 12-days period. They got an average RI of 1.454 at  $\lambda = 550$  nm and 1.460 at  $\lambda = 700$  nm wavelength excluding a nucleation event during they got unrealistic low (lower than  
5 the RI value of water) RI values. Our average RI values have a very good agreement with their average RI values, and this agreement is even better if we only compare our average  $RI_{\text{eff}}$  from January (1.446) with theirs.

If we look at the monthly averages, it is interesting to see, that in spite of the existing strong seasonal variability of both the aerosol concentration (Jaenicke et al., 1992; Weller et al., 2011) and chemical composition (Wagenbach et al., 1988) the RI does not or only slightly show the same behaviour: the monthly averages of  $RI_{\text{eff}}$  stay quite constant and remain within the  
10 range of 1.40–1.50. There are two winter months with higher RIs: July with a mean of 1.501 and September with 1.470. These values are significantly different from the yearly mean. In both of these months we have only relatively few data-points due to the extremely low concentrations and therefore we can only speculate on the reason for the slightly higher values. In winter the fraction of sea salt is higher than in summer and sea salt has a little bit higher RI than the other salts present in the aerosol phase (see more discussion in Sec. 3.5).

15 The monthly distributions are quite narrow, there is not a big scatter in the data. However, due to the needed long time averaging between 1 and 20 hours we might miss the possibly existing higher short-term variability. The winter months (June



to September) seem to have a higher scatter (Fig. 5 gray sticks), but this might be due to the higher uncertainty of the fitting method because of the extreme low concentrations and longer averaging time.

### 3.5 Link to the chemical composition

The average  $RI_{\text{eff}}$  of 1.438 is in a good agreement with what we would expect, if we look at the chemical composition of the aerosol at the SPUSO. The dominant aerosol component is sea-salt at this site, with around 50 % of the total mass in summer and 86 % in winter (Weller et al., 2008). Next to it, biogenic sulphur is also a very important component when it reaches its annual maximum in summer (Minikin et al., 1998). At our investigated wavelength of 633 nm, sea-salt has an RI of 1.49 (Shettle and Fenn, 1979), sulfuric acid 1.42 (Palmer and Williams, 1975), ammonium sulphate 1.53 (Toon et al., 1976), sodium nitrate 1.46 (Cotterell et al., 2017), ammonium nitrate 1.52 (Toon et al., 1976), MSA 1.43 (Virkkula et al., 2006) and black carbon 1.75+0.43i (Hess et al., 1998).

The chemical composition was determined from the daily filter measurements of the ionic composition and from the BC measurement of the MAAP. The mass concentration of the dominant component of sea salt was calculated from the  $Na^+$  ion. It was assumed that  $NH_4^+$  forms ammonium nitrate and the rest of  $NO_3^-$ , which cannot be neutralised, can be found as sodium nitrate. In the rare case when there is enough  $NH_4^+$  to completely neutralise the  $NO_3^-$ , the rest of the  $NH_4^+$  forms ammonium sulphate. The remaining  $SO_4^{2-}$  was assumed to be found as sulfuric acid. Using this chemical composition and assuming that the aerosol is homogeneously and internally mixed, the RI can be calculated from the volume fraction and the RI of the individual components. The imaginary part of the RI was again neglected, which is surely a justified assumption, because the volume fraction of the BC never exceeded 0.1 % in 2017.

The average RI calculated from the chemical composition in 2017 becomes 1.47, and as it was already mentioned, is in a good agreement with the optically retrieved  $RI_{\text{eff}}$  of 1.438. The slight difference may come next to the used assumptions from the fact that we used the bulk chemical composition to estimate the RI whereas we use only the size range between 120 and 340 nm for the fit and, as we will see later for a longer averaged time period (Section 3.7) that the RI changes slightly with the particle size.

If we average the chemical composition derived RI separately for the summer (November to February) and for the winter (March to October) we get slightly higher values for the austral winter with 1.482 than for the austral summer with 1.454. This is due the higher sea-salt fraction in winter, which has a higher RI among the components. This might explain as well why we have gained with the fitting procedure a slightly higher  $RI_{\text{eff}}$  values for two winter months.

### 3.6 Influence of the contamination

As we have already mentioned before the main station of Neumayer is a possible contamination source and we would like to investigate if this contamination source effects our derived  $RI_{\text{eff}}$  values or not. Therefore, first we check whether the actual wind direction influences our data and then we show a case study when diesel engines were operated right next to the measurement site.

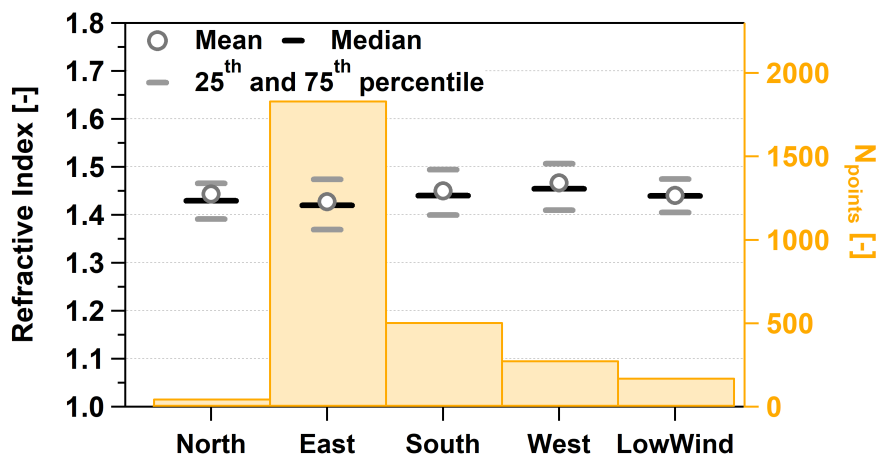


**Figure 6.** The averages, medians and percentiles of the  $RI_{\text{eff}}$  from the coastal Antarctica separated by the wind direction. The orange bars refer to the right axis and show the number of successful RI retrievals.

The prevailing wind direction at the SPUSO is east, often associated with high wind speeds over  $10 \text{ ms}^{-1}$ , and wind speeds over  $20 \text{ ms}^{-1}$  are restricted to this direction. The second frequent wind direction is south, but here the wind speeds are much lower, always stay below  $10 \text{ ms}^{-1}$  caused by katabatic flows. Westerly winds can also be present, even with moderate wind speeds between  $10$  and  $20 \text{ ms}^{-1}$ , but northerly winds are almost never present at the measurement site (König-Langlo et al., 1998). We have separated the  $RI_{\text{eff}}$  data according to the different wind direction sectors, in order to see if the different air-masses carry particles with different RI or not. We defined the wind direction sector between  $315^\circ$  and  $45^\circ$  as north,  $45^\circ$  and  $135^\circ$  as east,  $135^\circ$  and  $225^\circ$  as south and  $225^\circ$  and  $315^\circ$  as west. All the data with wind speeds below  $2 \text{ ms}^{-1}$  was categorized separately as a condition with low or no wind, and has the possibility that contamination reached the measurement site as well. Our measurement period was not exceptional: during most of the time when  $RI_{\text{eff}}$  could be retrieved, easterly winds were present (orange bars in Figure 6). We got many points during south and west wind, conditions with low wind did not occur often and only a very few points could be fit during winds coming from the northern sector, but we still have enough data points (49) to analyse them further.

Figure 6 shows the the  $RI_{\text{eff}}$  values sorted according to the wind direction. The gray circles show the time averages, the black sticks the medians, the gray sticks the 25<sup>th</sup> and 75<sup>th</sup> percentiles. We do not see any dependency of  $RI_{\text{eff}}$  on the wind direction,  $RI_{\text{eff}}$  seems to be stable and independent on from which direction the wind blew.

The main contamination source, the Neumayer station is situated 1.5 km north of the measurement site, therefore there is a possibility of contamination from this sector or for the cases when the wind speeds are very low. The contamination could origin from the diesel engines used for production of heat and electricity. This would be most probably associated with high concentrations of black carbon. Black carbon has an RI of  $1.75+0.43i$  (Hess et al., 1998) which is much higher than of any



other chemical components of the aerosol and has also a significant imaginary part. Therefore it is probable that in case of a present contamination the retrieved  $RI_{\text{eff}}$  gets higher as well.

Figure 6 does not show any elevated values for the cases when the wind is low or coming from north. Therefore we assume that we do not have any significant contamination even in these cases or the contamination did not cause any significant change of  $RI_{\text{eff}}$ . It is also possible, that exactly those situations could not fit successfully when contamination was present, however we did not even see an increased unsuccessful number of fits during winds from north or low wind speed values.

In order to further investigate the problem of the contamination we performed a case study from a period when planned contamination reached the SPUSO. This was the same construction event which was already shown in Fig. 4d as an example for an unsuccessful fit when the aerosol was changing too fast. On the day of 01.12.2017 diesel engine powered machines were in operation in the very close vicinity of the measurement site.

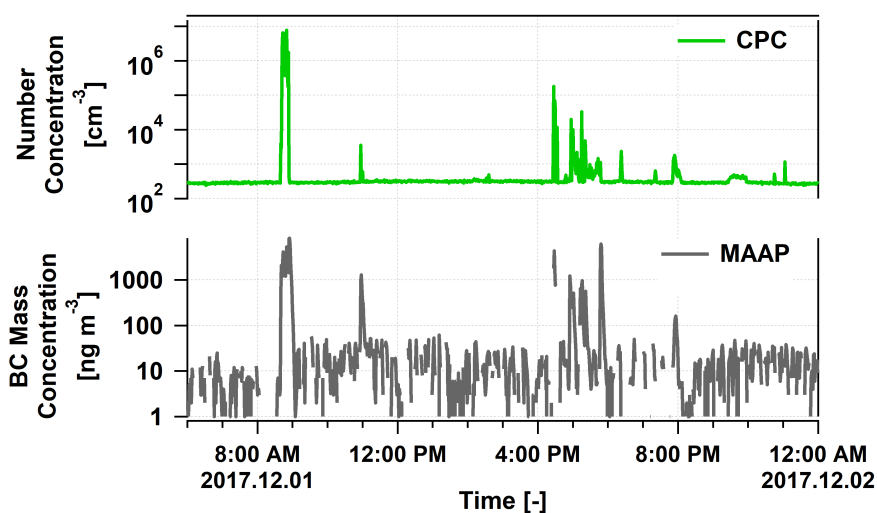


**Figure 7.** The particle number concentration (green) and the black carbon mass concentration (black) measured on 01.12.2017

Figure 7 shows the particle number concentration (green) and the black carbon mass concentration (black) as measured by the CPC and MAAP, respectively during this construction episode. The highest concentrations were present during the morning and the late afternoon even exceeding  $6 \times 10^6 \text{ cm}^{-3}$  and  $8 \mu\text{g m}^{-3}$  which are 3–4 orders of magnitude higher than the values without contamination (Weller et al., 2011, 2013). Unfortunately, these concentrations changed very fast, depending on whether the engine emissions were directly reaching our inlet and therefore most of the time, we were not able to perform a fit for the RI. We have only one single scan when the concentration was stable enough and elevated, that we can assume that we determined  $RI_{\text{eff}}$  for a contaminated situation.

Figure 8 shows this fit with the retrieved RI of 1.59. One can see that the original LAS scan fits already very well, which means that the RI of the factory calibration of PSLs give us a good solution. This retrieved  $RI_{\text{eff}}$  is significantly higher than the values we normally got. We can assume that the increased black carbon concentration caused this effect, and increased RI values

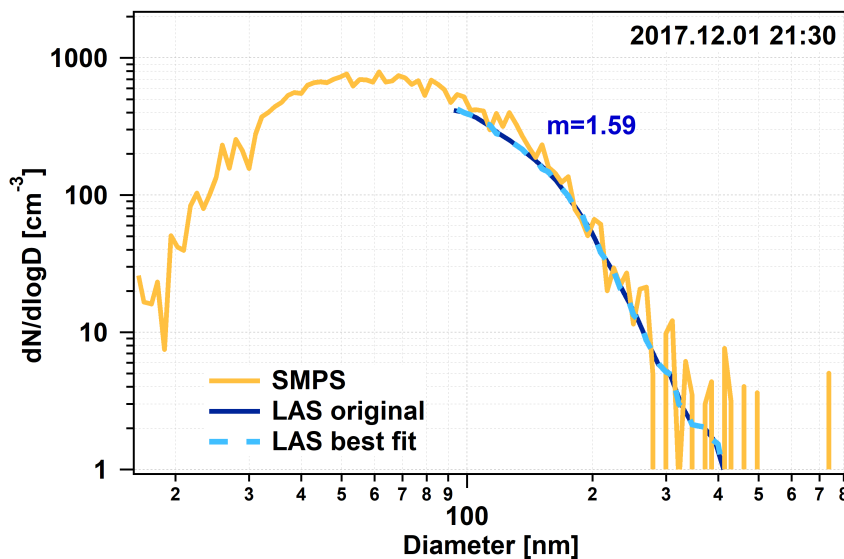


**Figure 8.** A successful fit from 01.12.2017 with high contamination present

might be an indicator for contamination at this site. This time period, and any other time period with known contamination was removed from the statistical calculations.

### 3.7 Size dependent contribution to the scattering

Having the data of the complete number size distribution (from 16 to 5000 nm) and the  $RI_{\text{eff}}$ , gives us the possibility to calculate the different sized particles' contribution to the scattering coefficient. Unfortunately, the LAS data was not usable above 600 nm during the time period when the particle losses were significant and therefore we can only do these calculations for an almost 2-months long summer period (01.12.2017-20.01.2018). It was assumed that the derived  $RI_{\text{eff}}$  is usable along the complete number size distribution (see section 3.8 where we speculate on the size dependence of the RI) and that the particles are spherical and the Mie calculation can be used for the determination of the single particle scattering at the wavelength of 633 nm. The scattering coefficient size distribution was calculated as follows:

$$\frac{d\sigma_s(D)}{d\log D} = C_s(D, \lambda, m) \cdot \frac{dN(D)}{d\log D} \quad (4)$$

where  $\sigma_s$  is the scattering coefficient,  $m$  is the derived, time dependent  $RI_{\text{eff}}$  and  $C_s$  is the scattering cross section of the particles.

Figure 9 shows the time average of  $d\sigma_s(D)/d\log D$  as function of the particle diameter. The cumulative distribution (dark green line, right axis) is also shown. As we can see, particles smaller than 100 nm or larger than 3  $\mu\text{m}$  do not contribute significantly to the scattering. 80% of the total scattering amount come from the size range between 208 and 1170 nm. Interestingly,

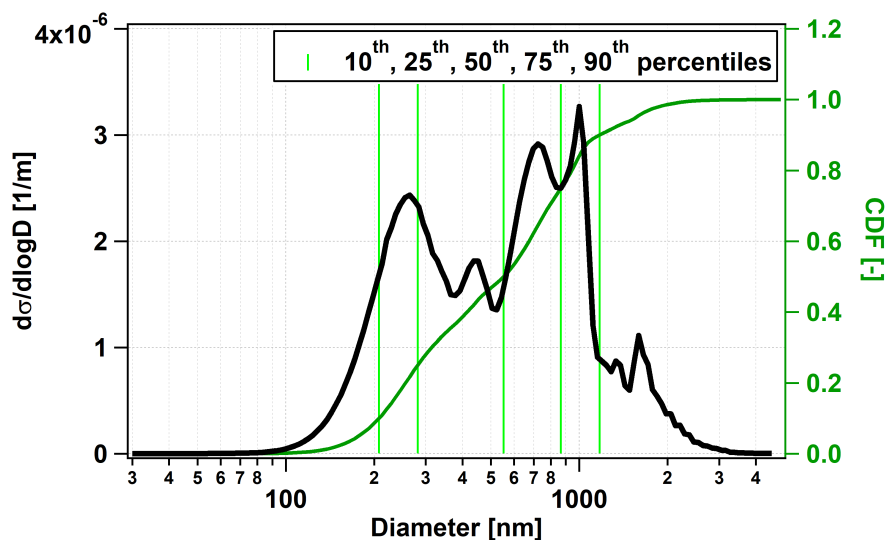


**Figure 9.** The scattering coefficient size distribution (black line) and the corresponding cumulative distribution (dark green line, right axis) as function of the particle diameter. The light green lines show the 10<sup>th</sup>, 25<sup>th</sup>, 50<sup>th</sup>, 75<sup>th</sup> and 90<sup>th</sup> of the distribution.

the distribution is multimodal, having two main peaks around 260 and 860 nm. The median of the distribution is at 550 nm which is much higher than the median of the number size distribution (64 nm), as expected.

### 3.8 Size dependence of the refractive index

We have a possibility to investigate the particle size dependence of the RI. We can only use again the time period (01.12.2017-20.01.2018) when the LAS was already repositioned and the particle losses were minimised. During this period we have an SMPS–LAS overlapping size range between 120 and 900 nm. If we calculate the time average for this complete time period, most of the noise will be averaged out as well, such that we can use this complete overlapping size range for the RI fit. This size range consists then of high enough measurements points such that it can be divided into more subranges and we can perform the RI fit separately in these. The resulted RI values will describe the particles with the particle sizes of the corresponding size range.

Figure 10 shows the time averaged LAS (gray line) and SMPS (black line) number size distributions. We have chosen the following particle size ranges for the separate RI fit and with this for the size dependency investigation: 117–168 nm, 168–241 nm, 241–346 nm, 376–478 nm and 478–710 nm. We have chosen these ranges such, that we have similar number of size distribution measurement points for the fit procedure in every range. The coloured lines in Figure 10 show the best RI<sub>eff</sub> fits.

With the increasing particle size we needed to apply a lower RI in order to have the best match between the LAS and the SMPS. In the first range we got an RI<sub>eff</sub> of 1.47, in the second 1.45, in the third 1.43, in the fourth 1.37 and in the fifth 1.30. According to this result the RI has a particle size dependence, and it is decreasing with the diameter in the investigated size range. The decrease in the first 3 size ranges is a slight decrease and getting steeper in the last two ranges.

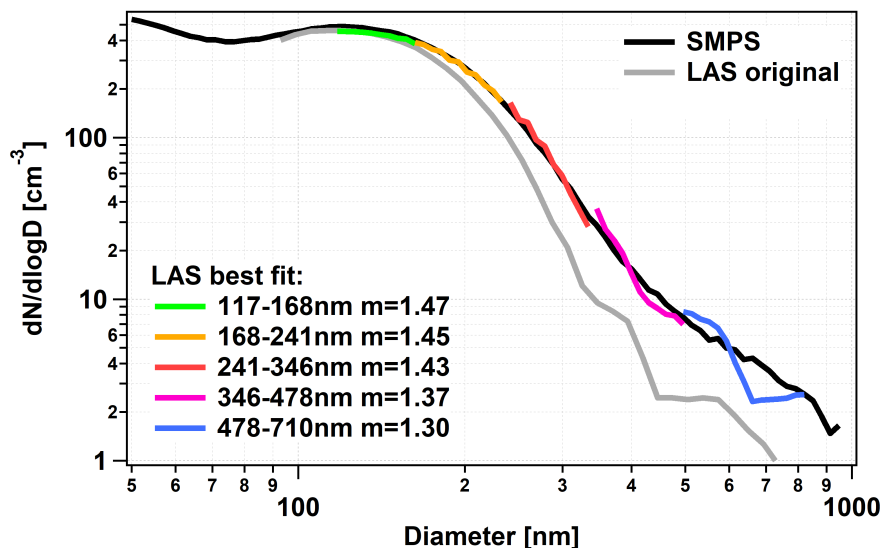


**Figure 10.** The average number size distribution measurements during December 2017 and January 2018 as measured by the SMPS (black line) and the LAS (gray line). The coloured lines show the 5 RI fitting procedures using 5 different particle size ranges.

The RI in the last diameter range of 478–710 nm became 1.30 which is surrealistically low, even lower than 1.33, the RI of water. We have to question the quality of the fit here, even looking at the fit with the naked eyes we see that even at the best choice of RI the LAS and the SMPS do not match well. The  $\chi$  value with 0.0018 is also close to the limit of 0.02 which was the limit we have set for the acceptance of a fit. One reason can be, that in this diameter range, the theoretical instrument response function is less steeper than for the lower diameters (See Figure 2) and therefore a small error in the measured scattering or in the polynomial fit of the TIR can already cause greater error in the diameter recalculation. Another possible explanation for the unrealistically low RI is the unusual shape of original LAS number size distribution in the highest chosen size range. The LAS number size distribution has a strange dip around 450 nm particle diameter. This dip is often present on the single scans as well, and we cannot think of any reasons why the size distribution should have such a shape and hence we think that it might be a systematical measurement error of the LAS. Therefore we consider the 1.30 RI value in the highest size range invalid.

#### 4 Conclusions

We have calculated the aerosol real RI at a coastal Antarctic measurement site using the overlapping size range of two instrument measuring the number size distribution in two different ways: optically and selecting the particles by their electrical mobility. The yearly average of the RI was calculated based on the data from almost a complete year and turned out to be 1.44. Based on this, we suggest this single, time constant refractive index value for optical modeling. It would be interesting to determine the geographical borders of this value's validity.



In spite of the seasonal variability of the aerosol at the measurement site, we could not identify a proper seasonal trend of the RI, which is in good agreement with what we assume from the filter based chemical composition. We could not find any significant influence from the wind direction either. Even those very few RI values, when the calculation was possible and the air was coming from the contaminated sector of the Neumayer station, were not different from the cases with other wind directions. We conclude therefore, that our data-set is not significantly influenced by contamination.

Unfortunately, most of the time the LAS was positioned too far away from the inlet and therefore suffered from too high particle losses. These losses could not be corrected for particle sizes larger than 600 nm and therefore the complete number size distribution until 5  $\mu\text{m}$  could be analysed and discussed only for a shorter summer period. During this period we could not measure the scattering coefficient because of our Nephelometer's failure. Therefore we could not perform an optical closure study between the number size distribution and the scattering coefficient using the calculated RIs. Future collected data will make this study possible.

*Data availability.* Data reported here are available at <https://doi.pangaea.de/10.1594/PANGAEA.899429> and <https://doi.pangaea.de/10.1594/PANGAEA.899430> for scientific purposes.

*Author contributions.* ZJ have performed the measurements, analysed and interpreted the data and wrote the manuscript. RW built up the measurement site, supervised the measurements and the data analysis and reviewed and edited the manuscript.

*Competing interests.* The authors declare that they have no conflict of interest.

*Acknowledgements.* The authors would like to thank all members of the 37<sup>th</sup> overwintering team of the Neumayer III station for their support and being a great group.



## References

- Barkey, B., Paulson, S. E., and Chung, A.: Genetic algorithm inversion of dual polarization polar nephelometer data to determine aerosol refractive index, *Aerosol Science and Technology*, 41, 751–760, <https://doi.org/10.1080/02786820701432640>, 2007.
- Barnard, J. C. and Harrison, L. C.: Monotonic responses from monochromatic optical particle counters, *Applied Optics*, 27, 584–592, <https://doi.org/10.1364/AO.27.000584>, 1988.
- Bluvshstein, N., Flores, J. M., Riziq, A. A., and Rudich, Y.: An approach for faster retrieval of aerosols' complex refractive index using cavity ring-down spectroscopy, *Aerosol Science and Technology*, 46, 1140–1150, <https://doi.org/10.1080/02786826.2012.700141>, 2012.
- Bukowiecki, N., Zieger, P., Weingartner, E., Jurányi, Z., Gysel, M., Neiningner, B., Schneider, B., Hueglin, C., Ulrich, A., Wichser, A., Henne, S., Brunner, D., Kaegi, R., Schwikowski, M., Tobler, L., Wienhold, F. G., Engel, I., Buchmann, B., Peter, T., and Baltensperger, U.: Ground-based and airborne in-situ measurements of the Eyjafjallajökull volcanic aerosol plume in Switzerland in spring 2010, *Atmospheric Chemistry and Physics*, 11, 10 011–10 030, <https://doi.org/10.5194/acp-11-10011-2011>, 2011.
- Cotterell, M. I., Willoughby, R. E., Bzdek, B. R., Orr-Ewing, A. J., and Reid, J. P.: A complete parameterisation of the relative humidity and wavelength dependence of the refractive index of hygroscopic inorganic aerosol particles, *Atmospheric Chemistry and Physics*, 17, 9837–9851, <https://doi.org/10.5194/acp-17-9837-2017>, 2017.
- Eidhammer, T., Montague, D. C., and Deshler, T.: Determination of index of refraction and size of supermicrometer particles from light scattering measurements at two angles, *Journal of Geophysical Research: Atmospheres*, 113, <https://doi.org/10.1029/2007JD009607>, 2008.
- Hand, J. L. and Kreidenweis, S. M.: A new method for retrieving particle refractive index and effective density from aerosol size distribution data, *Aerosol Science and Technology*, 36, 1012–1026, <https://doi.org/10.1080/02786820290092276>, 2002.
- Hess, M., Koepke, P., and Schult, I.: Optical properties of aerosols and clouds: the software package OPAC, *Bulletin of the American Meteorological Society*, 79, 831–844, [https://doi.org/10.1175/1520-0477\(1998\)079<0831:OPOAAC>2.0.CO;2](https://doi.org/10.1175/1520-0477(1998)079<0831:OPOAAC>2.0.CO;2), 1998.
- Hodkinson, J. R. and Greenfield, J. R.: Response calculations for light-scattering aerosol counters and photometers, *Applied Optics*, 4, 1463–1474, <https://doi.org/10.1364/AO.4.001463>, 1965.
- Hogan, A. W., Barnard, S., and Bortiniak, J.: Physical properties of the aerosol at the South Pole, *Geophysical Research Letters*, 6, 845–848, <https://doi.org/10.1029/GL006i011p00845>, 1979.
- IPCC: Technical Summary, p. 31–116, Cambridge University Press, <https://doi.org/10.1017/CBO9781107415324.005>, 2014.
- Jaenicke, R., Dreiling, V., Lehmann, E., Koutsenogui, P. K., and Stiglmayr, J.: Condensation nuclei at the German Antarctic station “Georg von Neumayer”, *Tellus B: Chemical and Physical Meteorology*, 44, 311–317, <https://doi.org/10.3402/tellusb.v44i4.15459>, 1992.
- Khlystov, A., Stanier, C., and Pandis, S. N.: An algorithm for combining electrical mobility and aerodynamic size distributions data when measuring ambient aerosol special issue of aerosol science and technology on findings from the fine particulate matter supersites program, *Aerosol Science and Technology*, 38, 229–238, <https://doi.org/10.1080/02786820390229543>, 2004.
- König-Langlo, G., King, J. C., and Pettré, P.: Climatology of the three coastal Antarctic stations Dumont d’Urville, Neumayer, and Halley, *Journal of Geophysical Research: Atmospheres*, 103, 10 935–10 946, <https://doi.org/10.1029/97JD00527>, 1998.
- Lohmann, U. and Feichter, J.: Global indirect aerosol effects: a review, *Atmospheric Chemistry and Physics*, 5, 715–737, <https://doi.org/10.5194/acp-5-715-2005>, 2005.
- Massie, S. and Hervig, M.: HITRAN 2012 refractive indices, *Journal of Quantitative Spectroscopy and Radiative Transfer*, 130, 373 – 380, <https://doi.org/https://doi.org/10.1016/j.jqsrt.2013.06.022>, HITRAN2012 special issue, 2013.



- Minikin, A., Legrand, M., Hall, J., Wagenbach, D., Kleefeld, C., Wolff, E., Pasteur, E. C., and Ducroz, F.: Sulfur-containing species (sulfate and methanesulfonate) in coastal Antarctic aerosol and precipitation, *Journal of Geophysical Research: Atmospheres*, 103, 10 975–10 990, <https://doi.org/10.1029/98JD00249>, 1998.
- Palmer, K. F. and Williams, D.: Optical constants of sulfuric acid - Application to the clouds of Venus, *Applied Optics*, 14, 208–219, <https://doi.org/10.1364/AO.14.000208>, 1975.
- Petzold, A. and Schönlinner, M.: Multi-angle absorption photometry—a new method for the measurement of aerosol light absorption and atmospheric black carbon, *Journal of Aerosol Science*, 35, 421 – 441, <https://doi.org/https://doi.org/10.1016/j.jaerosci.2003.09.005>, 2004.
- Pratte, P., Cosandey, S., and Goujon-Ginglinger, C.: A scattering methodology for droplet sizing of e-cigarette aerosols, *Inhalation Toxicology*, 28, 537–545, <https://doi.org/10.1080/08958378.2016.1224956>, 2016.
- Ramanathan, V., Crutzen, P. J., Kiehl, J. T., and Rosenfeld, D.: Aerosols, climate, and the hydrological cycle, *Science*, 294, 2119–2124, <https://doi.org/10.1126/science.1064034>, 2001.
- Schwartz, S. E.: The Whitehouse effect – short-wave radiative forcing of climate by anthropogenic aerosols: An overview, *Journal of Aerosol Science*, 27, 359–382, [https://doi.org/10.1016/0021-8502\(95\)00533-1](https://doi.org/10.1016/0021-8502(95)00533-1), 1996.
- Shepherd, R. H., King, M. D., Marks, A. A., Brough, N., and Ward, A. D.: Determination of the refractive index of insoluble organic extracts from atmospheric aerosol over the visible wavelength range using optical tweezers, *Atmospheric Chemistry and Physics*, 18, 5235–5252, <https://doi.org/10.5194/acp-18-5235-2018>, 2018.
- Shettle, E. P. and Fenn, R. W.: Models for the aerosols of the lower atmosphere and the effects of humidity variations on their optical properties, 1979.
- Toon, O. B., Pollack, J. B., and Khare, B. N.: The optical constants of several atmospheric aerosol species: Ammonium sulfate, aluminum oxide, and sodium chloride, *Journal of Geophysical Research*, 81, 5733–5748, <https://doi.org/10.1029/JC081i033p05733>, 1976.
- Valenzuela, A., Reid, J. P., Bzdek, B. R., and Orr-Ewing, A. J.: Accuracy required in measurements of refractive index and hygroscopic response to reduce uncertainties in estimates of aerosol radiative forcing efficiency, *Journal of Geophysical Research: Atmospheres*, 123, 6469–6486, <https://doi.org/10.1029/2018JD028365>, 2018.
- Virkkula, A., Koponen, I. K., Teinilä, K., Hillamo, R., Kerminen, V.-M., and Kulmala, M.: Effective real refractive index of dry aerosols in the Antarctic boundary layer, *Geophysical Research Letters*, 33, <https://doi.org/10.1029/2005GL024602>, 2006.
- Wagenbach, D., Görlach, U., Moser, K., and Münnich, K. O.: Coastal Antarctic aerosol: the seasonal pattern of its chemical composition and radionuclide content, *Tellus B: Chemical and Physical Meteorology*, 40, 426–436, <https://doi.org/10.3402/tellusb.v40i5.16010>, 1988.
- Weller, R., Wöltjen, J., Piel, C., Resenberg, R., Wagenbach, D., König-Langlo, G., and Kriews, M.: Seasonal variability of crustal and marine trace elements in the aerosol at Neumayer station, Antarctica, *Tellus B: Chemical and Physical Meteorology*, 60, 742–752, <https://doi.org/10.1111/j.1600-0889.2008.00372.x>, 2008.
- Weller, R., Minikin, A., Wagenbach, D., and Dreiling, V.: Characterization of the inter-annual, seasonal, and diurnal variations of condensation particle concentrations at Neumayer, Antarctica, *Atmospheric Chemistry and Physics*, 11, 13 243–13 257, <https://doi.org/10.5194/acp-11-13243-2011>, 2011.
- Weller, R., Minikin, A., Petzold, A., Wagenbach, D., and König-Langlo, G.: Characterization of long-term and seasonal variations of black carbon (BC) concentrations at Neumayer, Antarctica, *Atmospheric Chemistry and Physics*, 13, 1579–1590, <https://doi.org/10.5194/acp-13-1579-2013>, 2013.



- Wex, H., Petters, M. D., Carrico, C. M., Hallbauer, E., Massling, A., McMeeking, G. R., Poulain, L., Wu, Z., Kreidenweis, S. M., and Stratmann, F.: Towards closing the gap between hygroscopic growth and activation for secondary organic aerosol: Part 1 – Evidence from measurements, *Atmospheric Chemistry and Physics*, 9, 3987–3997, <https://doi.org/10.5194/acp-9-3987-2009>, 2009.
- Wiedensohler, A., Birmili, W., Nowak, A., Sonntag, A., Weinhold, K., Merkel, M., Wehner, B., Tuch, T., Pfeifer, S., Fiebig, M., Fjåraa, A. M., Asmi, E., Sellegri, K., Depuy, R., Venzac, H., Villani, P., Laj, P., Aalto, P., Ogren, J. A., Swietlicki, E., Williams, P., Roldin, P., Quincey, P., Hüglin, C., Fierz-Schmidhauser, R., Gysel, M., Weingartner, E., Riccobono, F., Santos, S., Grüning, C., Faloon, K., Beddows, D., Harrison, R., Monahan, C., Jennings, S. G., O’Dowd, C. D., Marinoni, A., Horn, H.-G., Keck, L., Jiang, J., Scheckman, J., McMurry, P. H., Deng, Z., Zhao, C. S., Moerman, M., Henzing, B., de Leeuw, G., Löschau, G., and Bastian, S.: Mobility particle size spectrometers: harmonization of technical standards and data structure to facilitate high quality long-term observations of atmospheric particle number size distributions, *Atmospheric Measurement Techniques*, 5, 657–685, <https://doi.org/10.5194/amt-5-657-2012>, 2012.
- World Meteorological Organisation, W.: WMO/GAW Aerosol Measurement Procedures, Guidelines and Recommendations, 2016.
- Zhang, X., Huang, Y., Rao, R., and Wang, Z.: Retrieval of effective complex refractive index from intensive measurements of characteristics of ambient aerosols in the boundary layer, *Opt. Express*, 21, 17 849–17 862, <https://doi.org/10.1364/OE.21.017849>, 2013.
- Zieger, P., Aalto, P. P., Aaltonen, V., Äijälä, M., Backman, J., Hong, J., Komppula, M., Krejci, R., Laborde, M., Lampilahti, J., de Leeuw, G., Pfüller, A., Rosati, B., Tesche, M., Tunved, P., Väänänen, R., and Petäjä, T.: Low hygroscopic scattering enhancement of boreal aerosol and the implications for a columnar optical closure study, *Atmospheric Chemistry and Physics*, 15, 7247–7267, <https://doi.org/10.5194/acp-15-7247-2015>, 2015.